PCCP

Accepted Manuscript

This article can be cited before page numbers have been issued, to do this please use: S. Chakrabarti, S. Maikap, S. Samanta, S. Jana, A. Roy and J. Qiu, *Phys. Chem. Chem. Phys.*, 2017, DOI: 10.1039/C7CP05089E.




ROYAL SOCIETY OF CHEMISTRY

rsc.li/pccp

View Article Online
DOI: 10.1039/C7CP05089E



# Scalable cross-point resistive switching memory and mechanism through understanding of $H_2O_2$/glucose sensing by using $IrO_x/Al_2O_3/W$ structure

Somsubhra Chakrabarti[1], Siddheswar Maikap[1,2,*], Subhranu Samanta[1], Surajit Jana[1], Anisha Roy[1], and Jian-Tai Qiu[2,3]

[1]*Thin Film Nano Tech. Lab., Department of Electronics Engineering, Chang Gung University, Tao-Yuan, 33302, Taiwan*

[2]*Division of Gyn-Oncology, Department of Obs/Gyn, Chang Gung Memorial Hospital (CGMH), Tao-Yuan, 33302, Taiwan*

[3]*Department of Biomedical Sciences, School of Medicine, Chang Gung University (CGU), Tao-Yuan, 33302, Taiwan*

*Corresponding author. Tel: 886 32118800 ext. 5785; Fax: 886 32118507.
*E-mail: sidhu@mail.cgu.edu.tw*

## Abstract

Resistive switching characteristics of scalable $IrO_x/Al_2O_3/W$ cross-point structure and mechanism through pH/$H_2O_2$ sensing along with glucose detection have been investigated for the first time. Porous $IrO_x$ and $Ir^{3+}/Ir^{4+}$ oxidation states are observed by high-resolution transmission electron microscope, field-emission scanning electron spectroscopy, and X-ray photo-electron spectroscopy. The 20 nm-thick $IrO_x$ devices in sidewall contact show consecutive long dc cycles at a low current compliance (CC) of 10 µA, multi-level operation with CC varies from 10 µA to 100 µA, and long program/erase endurance of $>10^9$ cycles with 100 ns pulse width. The $IrO_x$ with thickness of 2 nm in $IrO_x/Al_2O_3/SiO_2$/p-Si structure has shown super-Nernstian pH sensitivity of 115 mV/pH and detection of $H_2O_2$ in the range of 1-100 nM is also achieved owing to porous and reduction-oxidation (redox) of $IrO_x$ membrane, whereas pure $Al_2O_3/SiO_2$ membrane does not show $H_2O_2$ sensing. A simulation based on Schottky, hopping, Fowler-Nordheim tunneling conduction, and redox reaction is proposed. The experimental I-V curve is

View Article Online
DOI: 10.1039/C7CP05089E





matched very well with simulation. The resistive switching mechanism is owing to $O^{2-}$ ions migration and redox reaction of $Ir^{3+}/Ir^{4+}$ at the $IrO_x/Al_2O_3$ interface through $H_2O_2$ sensing as well as Schottky barrier height modulation is responsible. Glucose with a low concentration of 10 pM is detected by using a completely new process in $IrO_x/Al_2O_3/W$ cross-point structure. Therefore, this cross-point memory shows the method of low cost, scalable, memory with low current, multi-level operation, which will be useful for future highly dense three-dimensional (3D) memory and bio-sensor for future diagnosis of human diseases.

## Introduction

According to the recent progress of non-volatile memories, resistive random access memory (RRAM) is the most promising solution to handle the increasing demand of big data storage, owing to its simple structure, multi-level cell capability, and low power operation with low cost[1-4]. In addition, resistive switching characteristics in cross-point architecture are attracted attention due to its large connectivity of each cell to reach high-density application and to overcome the limitations of 3D Flash memory beyond 20 nm technology[5]. To achieve those above mentioned requirements, different materials such as, $TaO_x$ [6, 7], $HfO_x$ [8-10], and $TiO_x$ [11, 12] and different structures[13] have been reported. Different groups [8, 14, 15] have demonstrated technique to produce high-density memory cell. Bai et al. [14] and Yu et al. [15] have proposed 3D vertical structure, where Govoreanu et al. [8] have demonstrated 10 nm memory cell. However, those choices involve complex fabrication process and advance lithography technique. Multi-level operation is also an effective way to store high-density data, which have been reported with different structure like, $Pt/Ti/TiO_2/TiN$ [16] and $Pt/Ta_2O_5/TiN$ [17]. To encounter these above problems a cost effective technique is demonstrated in this report to physically scale down by using a simple $W/Al_2O_3/Ir$ structure. Although $Al_2O_3$ is one of the important switching materials because of its

View Article Online
DOI: 10.1039/C7CP05089E



larger energy gap (7.7 eV [18]) for useful of high resistance state (HRS), and lower Gibbs free energy ($\Delta G$ = -1582.3 kJ/mole [19]) for stable oxidation state. However, few reports [14, 20] with different structures have been observed recently. Bai et al. [14] have reported sidewall cross-point resistive switching phenomena using $Pt/AlO_\delta/Ta_2O_{5-x}/TaO_y/Pt$ device. However, scaling and conduction mechanism of a novel $W/Al_2O_3/Ir$ cross-point memory using Ir thickness scaling have not been reported yet. It is noted that Ir metal has been used for its metallic behavior even it is oxidized. So, the investigation of nanoscale memory device characteristics and $pH/H_2O_2$ sensing through Ir thickness have been demonstrated here. The resistive switching mechanism is still unclear, which is also one of the important issues. Therefore, the switching mechanism has been explored through $pH/H_2O_2$ sensing in electrolyte-insulator-semiconductor (EIS) structure with the same material as a sensing membrane is also investigated. In addition, glucose detection is an important to prevent hyperglucemia and hypoglucemia, which is investigated by using $IrO_x/Al_2O_3/W$ structure.

In this study, resistive switching memory characteristics in a simple $IrO_x/Al_2O_3/W$ cross-point at sidewall contact and resistive switching mechanism evolution through $pH/H_2O_2$ sensing in EIS structure have been reported for the first time. High-resolution transmission electron microscope (HRTEM) and field emission scanning electron microscope (FESEM) images show porous $IrO_x$ material. Multiple oxidation states of Ir are observed by X-ray photoelectron spectroscopy (XPS), which is responsible for redox reaction of Ir as well as $H_2O_2$ sensing mechanism. The 20 nm-thick devices perform multi-level cell (MLC) operation as well as reset current scaling with CCs varying from 10 μA to 100 μA. A simple current-voltage (I-V) simulation based on conduction mechanism and oxidation/reduction (redox) in RESET is presented. Memory device shows data retention of $>5\times10^4$ s with programming current varying

View Article Online
DOI: 10.1039/C7CP05089E



from 10 μA to 100 μA and excellent program/erase (P/E) endurance of $>10^9$ cycles at an operation current of 10 μA with 100 ns pulse width. The 2 nm-thick $IrO_x$ membrane in EIS structure shows super-Nernstian pH sensitivity of 115 mV/pH owing to porous $IrO_x$ film and $H_2O_2$ sensing is due to $Ir^{3+}/Ir^{4+}$ oxidation states. Glucose with low concentration of 10 pM is also sensed by using $IrO_x/Al_2O_3/W$ structure. The switching mechanism has been explored through $pH/H_2O_2$ sensing as well.

## Experimental

The 4-inch Si wafers were cleaned by Radio Corporation of America (RCA) method. First, a 200 nm-thick $SiO_2$ film was grown by wet oxidation process. Optical photolithography technique was used to pattern the electrodes with a width of 10 μm on $SiO_2$/Si substrate. Then, a 20 nm-thick $SiO_2$ layer was deposited by e-beam evaporator using $SiO_2$ granules. The deposition rate of $SiO_2$ film was 0.1 Å/s. The pressure of e-beam chamber during deposition was kept at $8 \times 10^{-6}$ Torr. Now, two types of RRAM devices were fabricated, one with $IrO_x/Al_2O_3/W$ structure (Device S1) and other with $W/Al_2O_3/IrO_x$ in sidewall contact (Device S2). To fabricate $IrO_x/Al_2O_3/W$ structure, after patterning the bottom electrode (BE) 200 nm-thick W was deposited by RF sputtering. The Ar flow, deposition pressure, and power were 5 sccm, 10 mTorr and 100 W, respectively. After lift-off and patterning the top electrode (TE), 20 nm-thick $Al_2O_3$ film as a switching material (SM) was deposited by RF sputtering. The Ar flow, deposition pressure, and power were 25 sccm, 30 mTorr, and 80 W, respectively. Then $IrO_x$ TE was deposited by RF sputtering. The Ar flow, $O_2$ flow, deposition pressure, and power were 25 sccm, 5 sccm, 20 mTorr, and 100 W, respectively. After lift-off we got the final structure of device S1. The SEM image of $2\times2$ cross-point structure of device S1 with a size of $10\times10$ $\mu m^2$ is given in Fig. 1(a). The zoom-in view of one cross-point is also given in Fig. 1(b), where the acquired BE

View Article Online
DOI: 10.1039/C7CP05089E



size is 10.52 μm and acquired TE size is 9.715 μm. The FE-SEM image of TE and BE is given in Fig. 1(c-d).

To fabricate W/$Al_2O_3$/$IrO_x$ structure in sidewall contact, iridium metal (Ir) electrode with a thickness of 20 nm was deposited by RF sputtering on $SiO_2$/Si substrate. The Ar flow, deposition pressure, and power were 25 sccm, 20 mTorr, and 100 W, respectively. Another $SiO_2$ layer with a thickness of approximately 50 nm was deposited by e-beam evaporator. This $SiO_2$ layer will help to have resistive switching in sidewall and to make isolation through top side in between the TE and BE. A lift-off process was performed to obtain the $IrO_x$ electrodes, which define the device sizes in nanoscale regime. In next step, second lithography was performed to etch $SiO_2$ from the $IrO_x$ pads for contact position. Third lithography step was used to pattern the other electrodes. Then, 20 nm-thick $Al_2O_3$ layer as a SM was deposited by RF sputtering. Deposition parameters were kept the same as SM of device S1. Then, tungsten (W) electrode with a thickness of approximately 200 nm was deposited by RF sputtering. Deposition parameters were kept the same as BE of device S1. Finally, lift-off process was performed to obtain the nanoscale W/$Al_2O_3$/$IrO_x$ cross-point memory devices (S2). The widths of the devices were varied from 4 to 50 μm but the thickness of $IrO_x$ electrode will control the device size. This concept can help to reach 20 nm device size, even our lithography/mask aligner can permit to have a size of more than 1000 nm. To study the physical scaling issue of the resistive switching memory device, this concept will be very useful for low cost high-density memory application. Fig. 1(e) represents the schematic view of the W/$Al_2O_3$/$IrO_x$ cross-point memory devices. The sidewall contact is shown in zoom-in view schematically also (Fig. 1(f)). TEM image shows a cross-sectional view of Ir with a typical thickness of 2 nm (Fig. 1(g)). Plane-view TEM images show porous Ir with thickness of 2 nm on $SiO_2$/Si substrate (Fig. 1(h)). At this low thickness, Ir

View Article Online
DOI: 10.1039/C7CP05089E



electrode is become $IrO_x$ due to residual oxygen. The HRTEM image of 2 nm-thick Ir film is shown in Fig. 1 (i). The sweeping bias was applied on the $IrO_x$ electrode and the W electrode was grounded during measurement. A typical device size of 20 μm×20 nm was generally measured. Switching characteristics were measured by using Agilent 4156C and B1500A semiconductor parameter/device analyzers. MATLAB was used to simulate I-V characteristics and to emphasize switching mechanism.

To fabricate pH sensor with the same $IrO_x$ materials on $Al_2O_3$ film, first Si wafer was cleaned by RCA method, then 40 nm-thick $SiO_2$ was grown by thermal oxidation in a furnace. The temperature was 950$^o$C and oxygen gas was introduced. Then, a 200 nm-thick Al was deposited on the back side of the wafer by thermal evaporation for metallic contact after cleaning by buffer oxide etching solution (BOE). Then post-metal annealing was done at 450$^o$C for 10 minutes in $N_2$ ambient (2.5 SLM $N_2$ flow). A 5 nm-thick $Al_2O_3$ membrane was deposited by rf sputtering with the same parameters as RRAM switching material. After that, a 2 nm-thick Ir (i.e., $IrO_x$) was deposited by RF sputtering with the same parameters as RRAM electrode. Then, a sensing area of 3.14 mm$^2$ was opened by lithography and lift-off process was performed. Each device was then cut and paste on the Cu printed circuit board (PCB) using Ag paste. Both Cu of the PCB and sensing area of the device were isolated by epoxy. To evaluate the effects of $IrO_x$, two types of EIS sensor were made; one with $Al_2O_3/SiO_2/Si$ structure (as-deposited and annealing at 450$^o$C for 10 min in $N_2$ ambient) and other with $IrO_x/Al_2O_3/SiO_2/Si$ structure. A schematic view of our novel electrolyte/$IrO_x/Al_2O_3/SiO_2$/p-Si structure (device S3) is shown in Fig. 2(a). Capacitance-voltage (C-V) measurement in pH solution ranging from pH2 to pH10 was performed by using HP 4184A *LCR* meter with 100 Hz frequency and the Ag/AgCl reference electrode was used. The pH/$H_2O_2$ solutions were bought from Alpha Aesar. The

View Article Online
DOI: 10.1039/C7CP05089E



reference voltage was taken at 50% of the accumulation capacitance. The device S1 was also used in detection of glucose. Firstly, 2 mM of TRIS buffer solution of pH value 7.4 was prepared by adjusting the pH value and commercial pH meter was used. Then 15 units of glucose oxidase enzyme was added into the solution. After that 5 ml, 1 mM glucose main stock was prepared. By diluting the main stock of 1mM glucose solution, glucose was added to the buffer plus enzyme solution successively to prepare 10 pM solution. Then the measurement is continued by putting 1uL drop of solution on the cross-point device and noticing the current value. The schematic view of measurement setup for the S1 cross-point devices is given in Fig. 2(b).

## Results and discussion

The analysis of XPS spectra of 2 nm-thick $IrO_x$ deposited on 5 nm-thick $Al_2O_3$ layer is given in Fig. 3. All spectra have been calibrated with respect to C*1s* peak centered at 284.7 eV. The Al2*p* spectrum is fitted at 74.3 eV owing to $Al_2O_3$ film (Fig. 3(a)). The spectra are fitted through subtracting the background by Shirley method each peak. Fang et al. [21] have reported similar binding energy peaks for Al2*p* spectra at 73.9 eV of atomic-layer-deposited 4.9 nm-thick $Al_2O_3$ film. Therefore, the film shows stoichiometric $Al_2O_3$. The $4f_{7/2}$ and $4f_{5/2}$ doublet spectra of Ir are given in Fig. 3(b). The Ir$4f_{7/2}$ and Ir$4f_{5/2}$ peaks are fitted at 61.8 eV and 64.9 eV, respectively. The Ir$4f_{7/2}$ and Ir$4f_{5/2}$ peaks are similar to the reported values of 61.9 eV and 65 eV respectively by Labou et al.[22] for sputtering deposited 500 nm-thick iridium-oxide. The de-convoluted peaks of Ir$4f_{7/2}$ are situated at 61.8 eV and 62.6 eV. These two peaks correspond to the $Ir^{3+}$ and $Ir^{4+}$ oxidation states. Similar values of 61.9 eV and 63.7 eV corresponding to $Ir^{3+}$ and $Ir^{4+}$ oxidation states are also reported [22]. The atomic concentrations of C*1s*, Si*2p*, Al*2p*, O*1s*, and Ir*4f* are 12.8, 2.6, 14.1, 61.0, and 9.5%, respectively. Fig. 3(c) shows the O*1s* spectrum, which is de-convoluted into three peaks at 530.5 eV, 531.3 eV, and 532.2 eV. These three oxygen peaks are

View Article Online
DOI: 10.1039/C7CP05089E



corresponding to $IrO_x$, $SiO_x$ (or hydroxide) and $SiO_2$ respectively. Mei et al. [23] have reported similar O*1s* peaks at 530.6 eV and 531.3 eV for oxide ($IrO_x$ or $Al_2O_3$) and hydroxide in 2 nm-thick sputter-deposited $IrO_x$ film. Nagpure et al. [24] have reported similar O*1s* peaks at 531.2 eV and 532.5 eV for $SiO_x$ and $SiO_2$ respectively in $SiO_2$ prepared by chemical method. The presence of multiple oxidation states and porous $IrO_x$ will be helpful for high pH sensitivity, which has been explained later.

Current-voltage (I-V) switching characteristics of the device S2 are shown in Fig. 4(a). The shadow lines represent 500 consecutive I-V cycles. The sweeping voltage is followed by arrows $0 \rightarrow +3$ V $\rightarrow 0 \rightarrow -3.5$ V $\rightarrow 0$. The current compliance is 10 µA. The set voltage ($V_{SET}$), reset voltage ($V_{RESET}$), and reset current ($I_{RESET}$) are found to be ~+2.3 V, ~-1 V, and ~20 µA, respectively. Device S2 shows good uniformity in cycle-to-cycle, which is also very essential for high-density memory application. The values of HRS and LRS at a 50% probability are found to be 18.59 MΩ and 133.67 kΩ, respectively. Good resistance ratio of 200 is observed. It is observed that the LRS value is decreased with increasing CC. In case of LRS, the conducting filament diameter increased with increasing CC, as investigated by simulation (Fig. 4(b)). In consequence, the $I_{RESET}$ values are decreased with decreasing the CCs from 100 µA to 10 µA. The average values of $I_{RESET}$ at CCs of 100, 50, 30 and 10 µA are found to be 53.1, 41.6, 18.3, and 16 µA, while the filament diameters as input parameter for simulation are 9.8, 8, 7.36, and 6.4 nm, respectively. It is observed that the $I_{RESET}$ values are lower as CC applied, owing to series resistance effect of Ir electrode. This could be useful as one-resistor (1R) without one-transistor with one-resistor (1T1R) or one-sector with one-resistor (1S1R) configuration. The advantage of this RRAM is that we can control the filament diameter, which helps to achieve very good $I_{RESET}$ scaling as well as scaling of RRAM. It is mentioned that this cross-point

View Article Online
DOI: 10.1039/C7CP05089E



memory is physically scalable up to 20 nm and the filament diameter as well as device size is found to be 6.4 nm from simulation. The device shows Schottky conduction in both the HRS and LRS currents at low field. The calculated values of $\varepsilon_r$ are found to be 7.3 and 7.8 for +Ve and –Ve bias of the HRS currents, respectively. Higashi et al. [25] have reported similar dielectric constant value of 7 in case of 20 nm-thick $Al_2O_3$ layer grown by atomic-layer-deposition. The calculated Schottky barrier height in HRS is about 0.6 eV. At LRS currents, the barrier heights are 0.42 eV and 0.5 eV for the +Ve and –Ve biases, respectively. The work functions ($\varphi$) of Ir and W are approximately 5 eV [19] and 4.32 eV [19], respectively and the electron affinity ($\chi$) of $Al_2O_3$ is 2.58 eV [26]. Due to higher difference in between metal work function and electron affinity of switching material ($\Phi_B=\varphi-\chi$), the Schottky barrier height at the $IrO_x/Al_2O_3$ interface is higher than the $W/Al_2O_3$ interface. At moderate field the HRS currents show hopping conduction [27, 28] with a hopping distance is about 0.23 nm, which value is within the range of reported hopping distances of 0.15-0.38 nm in $Al_2O_3$ film [29, 30]. The Fowler-Nordheim (F-N) tunneling fitting of the HRS currents in both -Ve and +Ve biases are given in Fig. 4(c). The barrier heights have been calculated from F-N fitting [7, 31] below,

$$\Phi_{F-N} = \frac{S_{F-N}^{2/3}}{3.6\times10^{6}} \qquad (1)$$

where, $S_{F\text{-}N}$ is the slope of the F-N ($\ln(J/E^2)$ Vs. 1/E) fitting. From equation (1), the $\Phi_{F\text{-}N}$ values are 0.36 eV and 0.27 eV for the –Ve and +Ve biases, respectively. The critical electric fields ($E_c$) are 3 MV/cm and 4.5 MV/cm for –Ve and +Ve biases, respectively. Those values are higher than the reported value of 2.6 MV/cm [32], which suggests the F-N tunneling phenomena. Experimental and simulated I-V characteristics with different CC of 10 μA are shown in Fig. 4(d). I-V curve is simulated by considering Schottky conduction at low field, hopping conduction at moderate

View Article Online
DOI: 10.1039/C7CP05089E



field, and F-N tunneling at high field of HRS, while LRS currents are considered Schottky conduction only. The drift-diffusion carrier continuity equation and Joule heat transfer equation in steady state [33] are used to simulate the RESET part. Different material parameters, such as hopping distance (0.22 nm), barrier height (0.6 eV), dielectric constant (7), density of state of conduction band ($8\times10^{24}$ [19]), frequency of thermal vibration ($1\times10^{13}$ Hz [34]), and activation energy (0.05 eV) are used in this simulation. The simulated I-V is matched well with experimental curve. This novel cross-point memory device shows multi-level data retention more than $5\times10^4$ s with operation current varying from 10 µA to 100 µA, given in Fig. 4(e). The LRS value decreases with increasing operation current. After $5\times10^4$ s, the memory device maintains a good resistance ratio of approximately 10 at an operation current of 10 µA. Both device S1 and S2 show more than $10^9$ cycles P/E endurance at low operation current with pulse width of 100 ns. Fig. 4(f) shows the P/E endurance of device S1 with operation current of 30 µA. Fig. 4(g) shows the P/E endurance of device S2 with a low operation current of 10 µA. This suggests that smaller size device (S2) has lower current operation, which shows potential of RRAM devices for nanoscale non-volatile memory application. The switching mechanism is also understood by sensing pH/$H_2O_2$ below.

Fig. 2(a) shows a schematic view of pH/$H_2O_2$ sensing by using 2 nm-thick $IrO_x$ in electrolyte-insulator-semiconductor structure. Fig. 5(a) shows C-V characteristics of $IrO_x$ membrane with pH2 to pH10 solutions (sensor S3). Similarly, the C-V characteristics of the annealing $Al_2O_3$ membrane are observed (Fig. 5(b)). The pH sensitivity (S) values are found to be 115 mV/pH, 56.7 mV/pH, and 26 mV/pH for the $IrO_x$, annealed $Al_2O_3$, and as-deposited $Al_2O_3$ membranes, respectively (Fig. 5(c)). The linearity ($R^2$) values are approximately 99.3%, 99%, and 97.3% for the $IrO_x$, annealed $Al_2O_3$, and as-deposited $Al_2O_3$ membranes, respectively.

View Article Online
DOI: 10.1039/C7CP05089E



Similar pH sensitivity values by using different sensing materials like $Ta_2O_5$ (56 mV/pH [35]), $HfO_2$ (52.3 mV/pH [36]), $TiO_2$ (56 mV/pH [37]), $GdO_x$ (53.2 mV/pH by our group [38]) are reported. Some other groups [39-41] also have reported pH sensing in the range of 50-80 mV/pH using 0.08-0.9 μm-thick iridium film by cyclic voltammetry, but pH sensitivity of a thin $IrO_x$ (2 nm) membrane on $Al_2O_3$ layer in EIS structure is obtained for the first time in this paper and this is much higher than other reported values. The values of reference voltage for pH2 to pH10 show positive for the $IrO_x$ membranes while those values are negative for both as-deposited and annealed $Al_2O_3$ membranes. This phenomenon is owing to higher φ value of Ir than the Al metal (5 eV vs. 4.32 eV). The reference voltage is shifted towards positive direction with increasing pH value for all the sensors because of de-protonation [42] of the sensing membranes or more adsorption of $OH^-$ ions with increasing pH value. On the other hand, the reference voltage is shifted towards negative direction owing to protonation ($H^+$ ions [42]) on the sensing membranes. The annealed $Al_2O_3$ membrane has higher pH sensitivity than the as-deposited one (56.7 mV/pH vs. 26 mV/pH, and this is due to annealed out defects from the films. However, the as-deposited $Al_2O_3$ film has been used for the RRAM memory devices. The $IrO_x$ film has been also deposited on as-deposited $Al_2O_3$ film. It is found that the $IrO_x$ membrane has shown super-Nernstian pH sensitivity (115 mV/pH) than those of other membranes. This is due to porous $IrO_x$ membrane and redox properties of the films. The pH sensitivity of 5 nm-thick $IrO_x$ membrane is approximately 50 mV/pH (data not shown here) owing to smaller pore size. On the other hand, the 2 nm-thick $IrO_x$ membrane has larger pore size (Fig. 1(i)) as well as this opens up more binding sites of $OH^-$ ions or $H^+$ ions on the surface or ion absorption is increased. It is also observed from four probe resistivity measurement that the resistivity of Ir rapidly decreased with increasing thickness from 2 nm to 20 nm (data not shown here). Chen et al. [43] have reported that

View Article Online
DOI: 10.1039/C7CP05089E



the resistivity of Pt is decreased with increasing the thickness from 5 nm to 25 nm. Therefore, for thicker Ir the sensing membrane is becoming a conducting plate and the capacitance value is drastically high, which is difficult to measure C-V characteristics properly by using our CV system as well as the pH sensitivity for the 10 nm- and 20 nm-thick $IrO_x$ membrane is unjustified. If the Ir thickness is 2 nm then it is also responsible for high pH sensitivity, which may be due to many oxidation states ($Ir^{3+}$ or $Ir^{4+}$) in Ir [44]. The oxidations states are also confirmed by both XPS characteristics (Fig. 3(b)) and $H_2O_2$ sensing (Fig. 5(d)). The $IrO_x$ membrane detects $H_2O_2$ with concentration ranging from 1-100 nM whereas the $Al_2O_3$ membrane does not sense $H_2O_2$. This indicates that the Al-O bonding is strong because of lower Gibbs free energy (-1582.3 kJ/mole [19]) and does not have catalytic activity in contact of $H_2O_2$. A strong catalytic activity is observed for the $IrO_x$ membrane owing to mixture of $Ir^{3+}$ and $Ir^{3+}$ oxidation states. In contact of $H_2O_2$, the $Ir^{3+}$ oxidation state changes to $Ir^{4+}$ oxidation state as observed in equation (2) below.

$$Ir^{3+} \longleftrightarrow Ir^{4+} + e^{-} \quad (2)$$

$$IrO_x \longleftrightarrow IrO_2 + e^{-} \quad (3)$$

Therefore, the $IrO_x$ membrane changes to $IrO_2$, as shown in equation (3). Basically, the work function of Ir increases with increasing concentration of $H_2O_2$. Kim et al. [45] have reported that the work function of Ir increases after plasma oxidation. Finally, the $H_2O_2$ is reduced to $H_2O$ ($H_2O_2 \rightarrow OH^* + OH^-$; $OH^* + e^- \rightarrow OH^-$; $OH^- + H^+ \rightarrow H_2O$). The $H^+$ ions are received from PBS buffer solution and produces $H_2O$, however, the pH values does not change in the solution. Therefore, the $Ir^{4+}$ ions are generated more with increasing $H_2O_2$ concentration as well as the reference voltage is shifted towards positive direction or the reference voltage shift increases

View Article Online
DOI: 10.1039/C7CP05089E



with increasing the $H_2O_2$ concentration. After oxidation of $IrO_x$ membrane by $H_2O_2$, this membrane can be reduced to $IrO_x$ if it is kept in PBS solution. The reduction-oxidation (redox) of the $IrO_x$ membrane is responsible to detect $H_2O_2$. We have fitted the voltage shift vs. $H_2O_2$ concentration curve, and the fitting equation is given below,

$$\rho = \exp\left[\frac{1}{m}\{\Delta V - V_0\}\right] \quad (4)$$

where, ρ is the concentration of $H_2O_2$, ΔV is the reference voltage shift, m is slope in the fitted curve, and $V_0$ is intercept of the curve in reference voltage shift axis. Similarly, the device S1 is also used to detect glucose. First, 1 μL of pH7 solution is dropped into the cross-point of device S1 in its HRS. Fig. 2(b) schematically describes the experimental procedure of measurement. Due to porous nature of $IrO_x$ (Fig. 1(i)) the solution is penetrated into the $IrO_x/Al_2O_3$ interface. The current-voltage characteristic is given in Fig. 5(e) with arrow directing the path. Both path 1 and 2 show Schottky nature with dielectric constant $\varepsilon_r$=10.17 in path 1 and $\varepsilon_r$=2 in path 2. The change in the value of $\varepsilon_r$ indicates the occurrence of reduction in path 1 and oxidation in path 2. After that, the current-time (I-t) characteristics of device S1 with pH7, Buffer plus enzyme and 10 pM glucose are measured (Fig. 5(f)). The current in I-t plot drops about 4.2 nA in case of 10 pM glucose with enzyme than buffer plus enzyme solution. Glucose reacts with glucose oxidase enzyme and produces $H_2O_2$ by following the equation (5) below.

$$D-glu\cos e + O_2 \xleftarrow{glu\cos e-oxidase} gluconic\ -acid\ (H^+) + H_2O_2 \quad (5)$$

This $H_2O_2$ oxidized $IrO_x$ to $IrO_2$ ($Ir^{3+} \rightarrow Ir^{4+}$). The barrier height at the $IrO_x/Al_2O_3$ interface increases due to $H_2O_2$ reaction as work function of $IrO_2$ is greater than that of $IrO_x$ [44]. Because of this reason the current value in device S1 is decreased due to glucose plus glucose-oxidase

View Article Online
DOI: 10.1039/C7CP05089E



enzyme solution. This specific glucose-oxidase enzyme reacts selectively with D-glucose only. Then, this produces $H_2O_2$ according to equation (5) as well as glucose is detected by the device. Therefore, glucose or enzyme with PBS buffer does not detect. However, glucose with enzyme in PBS buffer is detected. So the device shows high selectiveness towards glucose. Cella et al. [46] have reported 1 pM glucose detection using single-walled carbon nanotube-based chemiresistive affinity biosensors. Zhang et al. [47] have reported 1 nM glucose detection using cyclic voltammetry in $LaNi_{0.6}Co_{0.4}O_3$ modified electrode. Glucose detection of 1 μM by EIS structure using CdSe-ZnS nanoparticle is also reported by our group[48]. Therefore, the cross-point memory structure (S1) shows beneficial to have low concentration $H_2O_2$ detection. Glucose sensing using $IrO_x/Al_2O_3/W$ structure is reported for the first time in this paper and minimum detection of 10 pM with sensitivity ($\Delta I/I_0$) of 0.026/pM glucose (where $\Delta I=I_{10\ pM\ glucose}-I_0$, $I_0$ is the current at 0.5 s for PBS plus enzyme) is comparable or even much lower than other reported values (Table 1), which will be very useful for blood sugar detection with a small sample volume in near future.

Similar to the $H_2O_2$ sensing mechanism in device S3, the redox behavior of the $IrO_x$ electrode at the $IrO_x/Al_2O_3$ interface is also responsible for resistive switching mechanism. During SET (+2.3 V), the $O^{2-}$ ions are migrated towards $IrO_x/Al_2O_3$ interface and oxygen vacancy filament is formed at the $W/Al_2O_3$ interface as well as Schottky barrier height is reduced from 0.59 eV to 0.42 eV [Fig. 4(a)]. Due to intermixing of $Al_2O_3$ and Ir, the $IrO_x/Al_2O_3$ interface is more defective than the $Al_2O_3/W$ interface. In this situation, a thin oxygen-rich $IrO_x/Al_2O_3$ interface is formed or $Al^{1+}$ oxidation state is formed into the SM layer, and the electrons are tunneled through that interface. By applying negative bias, the Schottky barrier height at LRS current is slightly higher than the LRS current at negative bias (0.5 eV vs. 0.42 eV) owing to higher work function of Ir electrode. During RESET (-1.1 V), the $O^{2-}$ ions are migrated towards

View Article Online
DOI: 10.1039/C7CP05089E



the $W/Al_2O_3$ interface and the filament is oxidized or $Al^{2+}$ oxidation state is formed as well as Schottky barrier height is increased up to approximately -2 V. Further increase the negative voltage, the current increases up to -2.5 V due to changing the $Ir^{3+}$ to $Ir^{4+}$ oxidation state at the $IrO_x/Al_2O_3$ interface as well as work function of Ir increases. By increasing negative voltage of -3 V, the current decreases because the driven force is decreased. Similarly, Tappertzhofen et al.[52] have reported the Cu redox reaction in $Cu/SiO_2/Pt$ structure by using cyclic voltammetry. By sweeping back to negative voltage after -3 V, the electrons are tunneled through dissolution gap of the $Al_2O_3$ SM. Therefore, the switching mechanism is due to the $O^{2-}$ ions migration under external bias as well as Schottky barrier height modulation through redox reactions of SM ($Al^{1+}/Al^{2+}$) and $Ir^{3+}/Ir^{4+}$ oxidation states. This leads to repeatable I-V switching cycles at a low current operation as well as multi-level resistance states are observed. So this $Al_2O_3$-based RRAM structure is useful for both high density cross-point memory and bio-analytic detection.

## Conclusions

The scaling aspect by reducing $IrO_x$ thickness and resistive switching mechanism of $Al_2O_3$-based cross-point memory in a novel $W/Al_2O_3/IrO_x$ structure through $pH/H_2O_2$ sensing have been reported. The switching characteristics and glucose detection using $IrO_x/Al_2O_3/W$ structure are also reported. The FE-SEM images show $10\times10$ $\mu m^2$ $IrO_x/Al_2O_3/W$ cross-point structure with porous $IrO_x$ TE and HRTEM images indicate porous $IrO_x$ with a thinnest thickness of 2 nm. XPS spectra show the presence of $Ir^{3+}/Ir^{4+}$ oxidation states in $IrO_x$. The cross-point 20 nm-thick devices show switching repeatability of > 500 dc cycles at a low CC of 10 μA and multi-level operation at CCs varying from 10 μA to 100 μA. The I-V simulation based on Schottky, hopping and F-N tunneling conduction mechanism has been presented. Stable P/E endurance of $>10^9$ cycles at a low operation current of 10 μA is achieved with 100 ns pulse width along with multi-

View Article Online
DOI: 10.1039/C7CP05089E



level stable data retention. The $IrO_x$ sensing membrane show extremely high pH sensitivity of 115 mV/pH and $H_2O_2$ detection in range of 1-100 nM owing to porous and catalytic activity of the $IrO_x$ membrane. The resistive switching mechanism is due the conducting filament formation/rupture in the $Al_2O_3$ SM owing to $O^{2-}$ ions migration and redox reaction in the SM and $Ir^{3+}/Ir^{4+}$ oxidation states at the $IrO_x/Al_2O_3$ interface, which is changing the Schottky barrier height and HRS/LRS are observed. The $Ir^{3+}/Ir^{4+}$ oxidation states are also confirmed through $H_2O_2$ sensing. Glucose with low concentration of 10 pM is detected by a novel detection method using $IrO_x/Al_2O_3$/W cross-point MIM structure. Therefore, this cross-point memory device has extensive potential to achieve the requirement for low power, high-density non-volatile memory device application and bio-sensing for diagnosis of human diseases in near future.

## Author's contributions:

SC wrote the first draft. He analyzed data and simulated I-V curves. SS helped to analyze data and transport characteristics. SJ and AR measured pH and $H_2O_2$ sensing. JTQ explained the sensors. This research work was carried out under the instruction of SM. All the authors contributed to revise the manuscript. All authors read and approved the manuscript for publication.

## Conflicts of interests:

There are no conflicts to declare.

## Acknowledgments

This work was supported by Ministry of Science and Technology (MOST) Taiwan, under contract numbers: MOST-106-2221-E-182-075 and MOST-105-2221-E-182-002. The authors are grateful to Dr. Hsin-Ming Cheng and Ms. Ling-Na Tsai, Industrial

View Article Online
DOI: 10.1039/C7CP05089E



Technology Research Institute (ITRI), Hsinchu, Taiwan for measuring XPS spectra of our $IrO_x/Al_2O_3$ membrane on $SiO_2$/p-Si substrate.

## Reference:

1. L. O. Chua, Memristor—missing circuit element, *IEEE Trans. Circuit Theory*, 1971, **CT-18,** 507–519
2. F. Pan, S. Gao, C. Chen, C. Song and F. Zeng, Recent progress in resistive random access memories: Materials, switching mechanisms, and performance, *Mater. Sci. Eng. R Reports,* 2014, **83,** 1–59
3. A. C. Torrezan, J. P. Strachan, R. G. Medeiros and R. S. Williams, Sub-nanosecond switching of a tantalum oxide memristor *Nanotechnology,* 2011, **22,** 485203
4. A. Prakash, D. Jana and S. Maikap, $TaO_x$-based resistive switching memories: prospective and challenges, *Nanoscale Res. Lett.* 2013, **8,** 418
5. W. Kim, S. Choi, J. Sung, T. Lee, C. Park, H. Ko, J. Jung, I. I. YooI and Y. Park, Multi-layered vertical gate NAND flash overcoming stacking limit for terabit density storage, *Dig. Tech. Symp. VLSI Tech.,* 2009, 188
6. Z. Wei and K. Eriguchi, Analytic modeling for nanoscale resistive filament variation in ReRAM with stochastic differential equation, *IEEE Trans. Electron Devices,* 2017, **64,** 2201–6
7. Z. Wang, J. Kang, Z. Yu, Y. Fang, Y. Ling, Y. Cai, R. Huang and Y. Wang, Modulation of nonlinear resistive switching behavior of a $TaO_x$-based resistive device through interface engineering, *Nanotechnology,* 2017, **28,** 55204

View Article Online
DOI: 10.1039/C7CP05089E



8. B. Govoreanu, G. S. Kar, Y. Y. Chen, V. Paraschiv, S. Kubicek, A. Fantini, I. P. Radu, L. Goux, S. Clima, R. Degraeve, N. Jossart, O. Richard, T. Vandeweyer, K. Seo, P. Hendrickx, G. Pourtois, H. Bender, L. Altimime, D. J Wouters, J. A. Kittl and M. Jurczak, 10×10 $nm^2$ $Hf/HfO_x$ crossbar resistive RAM with excellent performance, reliability and low-energy operation, *IEDM,* 2011, 31.6.1-31.6.4

9. S. Z. Rahaman, Y. D. Lin, H. Y. Lee, Y. S. Chen, P. S. Chen, W. S. Chen, C. H. Hsu, K. H. Tsai, M. Tsai and P. H Wang, The role of Ti buffer layer thickness on the resistive switching properties of hafnium oxide-based resistive switching memories, *Langmuir,* 2017, **33**, 4654-4665

10. K. S. Li, C. Ho, M. T. Lee, M. C. Chen, C. L. Hsu, J. M. Lu, C. H. Lin, C. C. Chen, B. W. Wu, Y. F. Hou, C. Y. Lin, Y. J Chen, T. Y. Lai, M. Y. Li, I. Yang, C. S. Wu and F. L. Yang, Utilizing sub-5 nm sidewall electrode technology for atomic-scale resistive memory fabrication, *Dig. Tech. Symp. VLSI Tech.,* 2014, 1-2

11. D. Carta, I. Salaoru, A. Khiat, A. Regoutz, C. Mitterbauer, N. M. Harrison and T. Prodromakis, Investigation of the switching mechanism in $TiO_2$-based RRAM: a two-dimensional EDX approach, *ACS Appl. Mater. Interfaces,* 2016, **8,** 19605

12. D. Panda, A. Dhar and S. K. Ray, Non-volatile memristive switching characteristics of $TiO_2$ films embedded with nickel nanocrystals," *IEEE Trans. Nanotechnology*, 2012, **11**, 51.

13. N. Gogurla, S. P. Mondal, A. K. Sinha, A. K. Katiyar, W. Banerjee, S. C. Kundu and S.. K. Ray, Transparent and flexible resistive switching memory devices with very high ON/OFF ratio using gold nanoparticles embedded in silk protein matrix, *Nanotechnology,* 2013, **24**, 345202.

View Article Online
DOI: 10.1039/C7CP05089E



14. Y. Bai, H. Wu, R. Wu, Y. Zhang, N. Deng, Z. Yu and H. Qian, Study of multi-level characteristics for 3D vertical resistive switching memory, *Sci. Rep.,* 2015, **4,** 5780

15. M. Yu, Y. Cai, Z. Wang, Y. Fang, Y. Liu, Z. Yu, Y. Pan, Z. Zhang, J. Tan, X. Yang, M. Li and R. Huang, Novel vertical 3D structure of $TaO_x$-based RRAM with self-localized switching region by sidewall electrode oxidation, *Sci. Rep.,* 2016, **6,** 1–10

16. F. Lentz, B. Roesgen, V. Rana, D. J. Wouter and R. Waser, Current compliance-dependent nonlinearity in $TiO_2$ ReRAM, *IEEE Electron Device Lett.,* 2013, **34,** 996–8

17. W. Hu, L. Zou, C. Gao, Y. Guo and D. Bao, High speed and multi-level resistive switching capability of $Ta_2O_5$ thin films for nonvolatile memory application, *J. Alloys Compd.,* 2016, **676,** 356–60

18. E. O. Filatova and A. S. Konashuk, Interpretation of the changing the band gap of $Al_2O_3$ depending on its crystalline form: connection with different local symmetries, *J. Phys. Chem. C,* 2015, **119,** 20755–61

19. R. C. Weast (ed.), CRC Handbook of Chemistry and Physics, 64 ed., CRC Press, Taylor and Francis Group, New York, 1984.

20. S. Kim and B. G. Park, Nonlinear and multilevel resistive switching memory in $Ni/Si_3N_4/Al_2O_3/TiN$ structures, *Appl. Phys. Lett.,* 2016, **108,** 212103

21. R. C. Fang, Q. Q. Sun, P. Zhou, W. Yang, P. F. Wang and D. Zhang, High-performance bilayer flexible resistive random access memory based on low-temperature thermal atomic layer deposition, *Nanoscale Res. Lett.,* 2013, **8,** 92

22. D. Laboua, E. Slavcheva, U. Schnakenberg and S. Neophytides, Performance of laboratory polymer electrolyte membrane hydrogen generator with sputtered iridium oxide anode, *J. Power Sources*, 2008, **185,** 1073-1078.

View Article Online
DOI: 10.1039/C7CP05089E



23. B. Mei, B. Seger, T. Pedersen, M. Malizia, O. Hansen, I. Chorkendorff and P. C. K. Vesborg, Protection of $p^+$-n-Si Photoanodes by sputter-deposited Ir/$IrO_x$ thin films, *J. Phys. Chem. Lett.,* 2014, **5,** 1948–52

24. I. M. Nagpure, S. S. Pitale, K. G. Tshabalala, V. Kumar, O. M. Ntwaeaborwa, J. J. Terblans and H. C. Swart, Luminescence response and CL degradation of combustion synthesized spherical $SiO_2$:Ce nanophosphor, *Mater. Res. Bull.*, 2011, **46**, 2359.

25. G. S. Higashi and C. G. Fleming, Sequential surface chemical reaction limited growth of high quality $Al_2O_3$ dielectrics, *Appl. Phys. Lett.,* 1989, **55,** 1963

26. M. L.Huang, Y. C. Chang, C. H. Chang, T. D. Lin, J. Kwo, T. B. Wu and M. Hong, Energy-band parameters of atomic-layer-deposition $Al_2O_3$/InGaAs heterostructure, *Appl. Phys. Lett.,* 2006, **89,** 87–90

27. D. Jana, S. Samanta, S. Maikap and H. M. Cheng, Evolution of complementary resistive switching characteristics using $IrO_x$/$GdO_x$/$Al_2O_3$/TiN structure, *Appl. Phys. Lett.,* 2016, **108** 011605

28. N. F. Mott, E. A. Davis, Electronic processes in non-crystalline materials, Oxford university press, New York 1971.

29. A. B. Belonoshko, A. Rosengren, Q. Dong, G. Hultquist and C. Leygraf, First-principles study of hydrogen diffusion in α-$Al_2O_3$ and liquid alumina, *Phys. Rev. B,* 2004, **69,** 115409

30. H. J. Xiang, J. L. F. DaSilva, H. M. Branz and S. H. Wei, Understanding the clean interface between covalent si and ionic $Al_2O_3$, *Phys. Rev. Lett.,* 2009, **103,** 2–5

31. R. H. Fowler and L. Nordheim, Electron emission in intense electric fields, *Proc. Royal*

View Article Online
DOI: 10.1039/C7CP05089E

*Soc. A,* 1928, **119,** 173

32. F. C. Chiu, Interface characterization and carrier transportation in metal/$HfO_2$/silicon structure, *J. Appl. Phys.,* 2006, **100,** 114102
33. S. Chakrabarti, S. Samanta, S. Maikap, S. Z. Rahaman and H. M. Cheng, Temperature-dependent non-linear resistive switching characteristics and mechanism using a new W/$WO_3$/$WO_x$/W structure, *Nanoscale Res. Lett.,* 2016, **11,** 389
34. A. M. Stoneham, Ionic Solids at High Temperatures, World Scientific Publishing Co. Pvt., Ltd., Singapore, 1989.
35. M. Chen, Y. Jin, X. Qu, Q. Jin and J. Zhao, Electrochemical impedance spectroscopy study of $Ta_2O_5$ based EIOS pH sensors in acid environment, *Sensors Actuators, B Chem.,* 2014, **192,** 399–405
36. Y. T. Lin, C. S. Huang, L. Chow, J. M. Lan, C. M. Yang, L. B. Chang and C. S. Lai, Light-immune pH sensor with SiC-based electrolyte-insulator-semiconductor structure, *Appl. Phys. Express,* 2013, **6,** 127002
37. P. K. Shin, The pH-sensing and light-induced drift properties of titanium dioxide thin films deposited by MOCVD, *Appl. Surf. Sci.,* 2003, **214,** 214–21
38. P. Kumar, S. Maikap, S. Ginnaram, J. Qiu, D. Jana, S. Chakrabarti, S. Samanta, K. Singh, A. Roy, S. Jana, M. Dutta, Y. Chang, H. Cheng, R. Mahapatra, H. Chiu and J. Yang, Cross-point resistive switching memory and urea sensing by using annealed $GdO_x$ Film in $IrO_x$/$GdO_x$/W Structure for Biomedical Applications, *J. Electrochem. Soc.* 2017*,* **164,** B127-B135

View Article Online
DOI: 10.1039/C7CP05089E



39. C. M. Nguyen, W. D. Huang, S. Rao, H. Cao, U. Tata, M. Chiao and J. C. Chiao, Sol-gel iridium oxide-based pH sensor array on flexible polyimide substrate, *IEEE Sens. J.,* 2013, **13,** 3857–64

40. F. Huang, Y. Jin, L. Wen, D. Mu and M. Cui, Effects of thermal oxidation cycle numbers and hydration on $IrO_x$ pH Sensor, *J. Electrochem. Soc.,* 2013, **160,** B184–B191

41. W. Olthuis, M. A. M. Robben, P. Bergveld, M. Bos and W. E. V. D. Linden, pH sensor properties of electrochemically grown iridium oxide, *Sensors Actuators B. Chem.,* 1990, **2,** 247–56

42. G. Zheng, F. Patolsky, Y. Cui, W. U. Wang and C. M. Lieber, Multiplexed electrical detection of cancer markers with nanowire sensor arrays, *Nat. Biotechnol.,* 2005, **23,** 1294–301

43. H. Y. Chen, S. Yu, B. Gao, R. Liu, Z. Jiang, Y. Deng, B. Chen, J. Kang and H. S. P. Wong, Experimental study of plane electrode thickness scaling for 3D vertical resistive random access memory, *Nanotechnology* 2013, **24,** 465201

44. P. Pyykko and W. H. Xu,The formal oxidation states of iridium now run from -III to +IX, *Angew. Chemie-Int. Ed.,* 2015, **54,** 1080–1

45. S. Y. Kim, J. L. Lee, K. B. Kim, Y. H. Tak, Enhancement of hole injection using iridium-oxide-coated indium tin oxide anodes in organic light-emitting diodes, *Appl. Phys. Lett.,* 2005, **86,** 133504.

46. L. N. Cella, W. Chen, N. V. Myung, and A. Mulchandani, Single-walled carbon nanotube-based chemiresistive affinity biosensors for small molecules: ultrasensitive glucose detection, *J. Am. Chem. Soc.*, 2010, **132**, 5024–5026.

View Article Online
DOI: 10.1039/C7CP05089E



47. Z. Zhang, S. Gu, Y. Ding and J. Jin, A novel nonenzymatic sensor based on $LaNi_{0.6}Co_{0.4}O_3$ modified electrode for hydrogen peroxide and glucose, *Anal. Chim. Acta*, 2012, **745**, 112-117.

48. P. Kumar, S. Maikap, K. Singh, S. Chatterjee, Y. Y. Chen, H. M. Cheng, J. T. Qiu and J. R. Yang, Highly reliable label-free detection of urea/glucose and sensing mechanism using $SiO_2$ and CdSe-ZnS nanoparticles in electrolyte-insulator-semiconductor structure, *J. Electrochem. Soc.*, 2016, **163**, B580-B587.

49. G. Slaughter and T. Kulkarni, Highly selective and sensitive self-powered glucose sensor based on capacitor circuit, *Sci. Rep.*, 2017, **7**, 1471.

50. J. Hea, J. Sunarso, Y. Zhu, Y. Zhong, J. Miao, W. Zhou and Z. Shao, High-performance non-enzymatic perovskite sensor for hydrogen peroxide and glucose electrochemical detection, *Sens. Actuator B-Chem*, 2017, 244, 482.

51. D. Xu, L. Luo, Y. Ding and P. Xu, Sensitive electrochemical detection of glucose based on electrospun $La_{0.88}Sr_{0.12}MnO_3$ naonofibers modified electrode, *Anal. Biochem*., 2015, 489, 38.

52. S. Tappertzhofen, H. Mündelein, I. Valov, R. Waser, Nanoionic transport and electrochemical reactions in resistively switching silicon dioxide, *Nanoscale,* 2012, **4,** 3040.

## Figure Captions

**Figure 1. (a)** SEM view of the 2×2 cross-points using $IrO_x/Al_2O_3/W$ structure (S1). **(b)** zoom-in view of 10×10 $\mu m^2$ cross-point. The FE-SEM view of **(c)** W BE and **(d)** $IrO_x$ TE. The W shows large grain size and $IrO_x$ shows porous structure. **(e)** Schematic view of cross-point memory using novel $W/Al_2O_3/IrO_x$ structure in sidewall contact (S2). Physical size of the device is

View Article Online
DOI: 10.1039/C7CP05089E



reduced by thickness of $IrO_x$ to 20 nm. **(f)** The sidewall contact is depicted by schematically in zoom-in view. **(g)** Cross-sectional TEM image shows $IrO_x$ with a typical thickness of 2 nm in $SiO_2$/p-Si substrate and corresponding **(h)** plane-view TEM image and **(i)** HRTEM images show porous $IrO_x$.

**Figure 2. (a)** Schematic view of electrolyte/$IrO_x$/$Al_2O_3$/$SiO_2$/p-Si structure on a PCB. The Ag/AgCl reference electrode has shown. **(b)** Schematic of experimental setup of glucose detection by using $IrO_x$/$Al_2O_3$/W cross-point structure.

**Figure 3.** XPS spectra showing the binding energy of (a) Al 2*p*, (b) Ir 4*f*, and (c) O 1*s* electrons.

**Figure 4. (a)** Consecutive 500 I-V switching curves at a low CC of 10 μA are shown for the 20 nm-thick $IrO_x$ devices (S2). **(b)** Both reset current and filament diameter are decreased with decreasing CCs from 100 μA to 10 μA. **(c)** F-N tunneling fitting of the HRS currents in both –Ve and +Ve biases is plotted. **(d)** Simulated I-V curve with 10 μA CC is well fitted with experimental result. **(e)** Stable data retention characteristics of > $5\times10^4$ s with CCs varying from 10-100 μA are obtained. **(f)** P/E endurance of >$10^9$ cycles with 100 ns pulse width of $IrO_x$/$Al_2O_3$/W (S1) and **(g)** W/$Al_2O_3$/$IrO_x$ (S2) cross-point memory devices. The sidewall contact devices show long P/E endurance of >$10^9$ cycles even at low 10 μA P/E current.

**Figure 5.** C-V characteristics with pH2 to pH10 for the **(a)** $IrO_x$ and **(b)** annealed $Al_2O_3$ membranes. **(c)** pH sensitivity characteristics of the $IrO_x$, annealed $Al_2O_3$, and as-deposited $Al_2O_3$ membranes. **(d)** The reference voltage shift with $H_2O_2$ concentration as well as a new fitting equation is developed. **(e)** I-V characteristic of $IrO_x$/$Al_2O_3$/W cross-point structure with pH7 (S1). This shows Schottky like characteristics. (f) Current-time response of $IrO_x$/$Al_2O_3$/W cross-point device with buffer and low concentration of 10 pM glucose is detected.

View Article Online
DOI: 10.1039/C7CP05089E



## Table Captions

**Table 1. Comparison of glucose sensitivity and detection limit by using our $IrO_x/Al_2O_3/W$ resistive switching structure and best published results in literature.** (MWCNT: Multi-wall carbon nano-tube; PQQ-GDH: pyrroloquinoline quinone glucose dehydrogenase; LSC: $La_{0.6}Sr_{0.4}CoO_{3-\delta}$; RGO: reduced graphene oxide; CPE: carbon paste electrode; LCMO: $La_{0.88}Sr_{0.12}MnO_3$; LNC: $LaNi_{0.6}Co_{0.4}O_3$; SWCNT: Single wall CNT; FET: field-effect-transistor)

| Structure | Sensing material | Sensitivity | Minimum detection value | Ref. |
|---|---|---|---|---|
| $IrO_x/Al_2O_3/W$ resistive switching | $IrO_x$ | 0.026/pM glucose | 10 pM | This work |
| MWCNTs electrode | PQQ-GDH | 23.12 Hz $mM^{-1}cm^2$ | 1 mM | [49] |
| LSC electrode | RGO | 330 µA $mM^{-1}cm^{-2}$ | 63 nM | [50] |
| LCMO electrode | CPE | 1111.1 µA $mM^{-1}$ $cm^{-2}$ | 31.2 nM | [51] |
| LNC electrode | CPE | 1812.84 µA $mM^{-1}cm^{-2}$ | 1 nM | [47] |
| SWCNT-FET | SWCNT | 0.039/pM glucose | 1 pM | [46] |

View Article Online
DOI: 10.1039/C7CP05089E



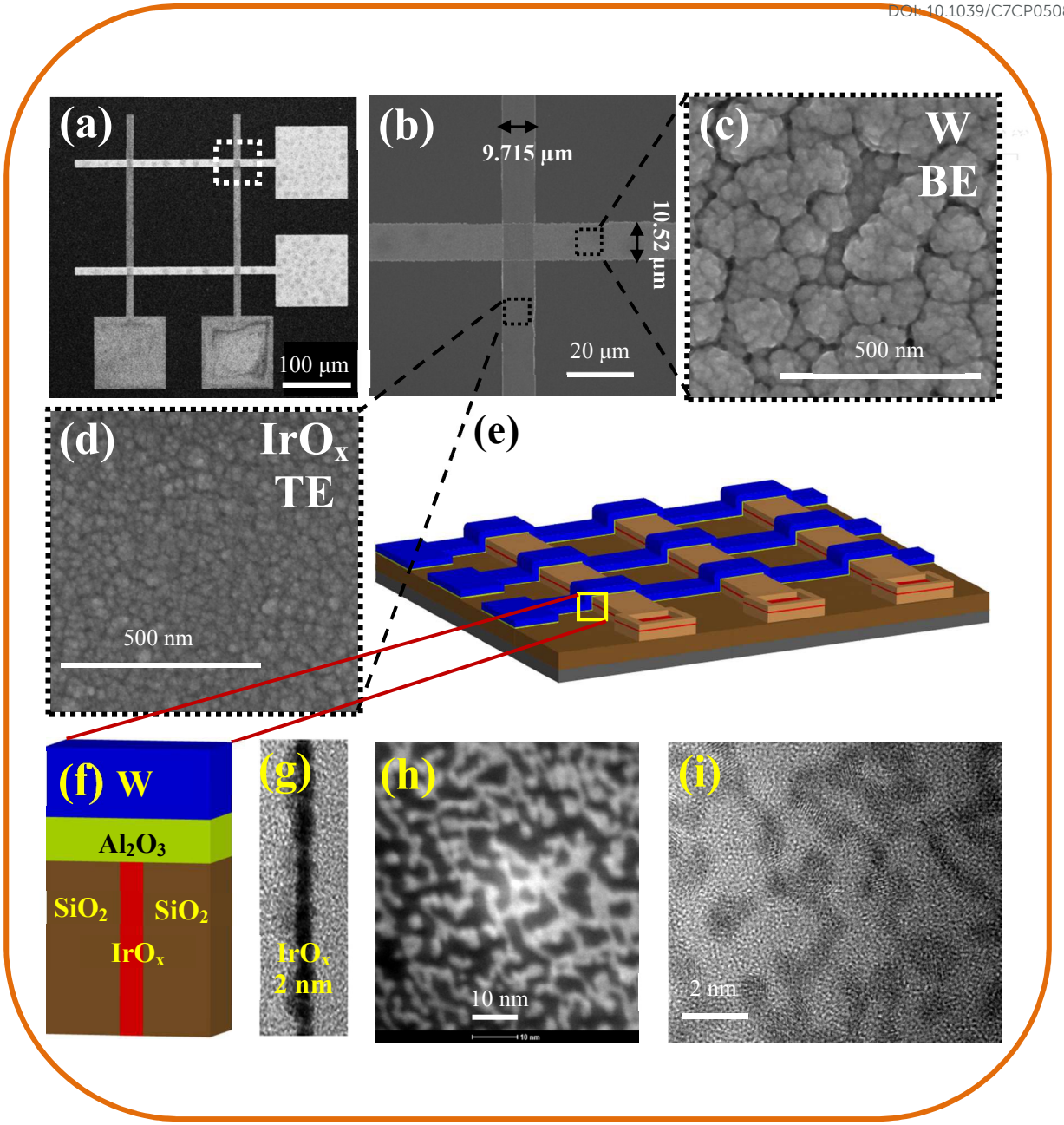


**Fig. 1. S. Chakrabarti et al., PCCP, September, 2017**

View Article Online
DOI: 10.1039/C7CP05089E



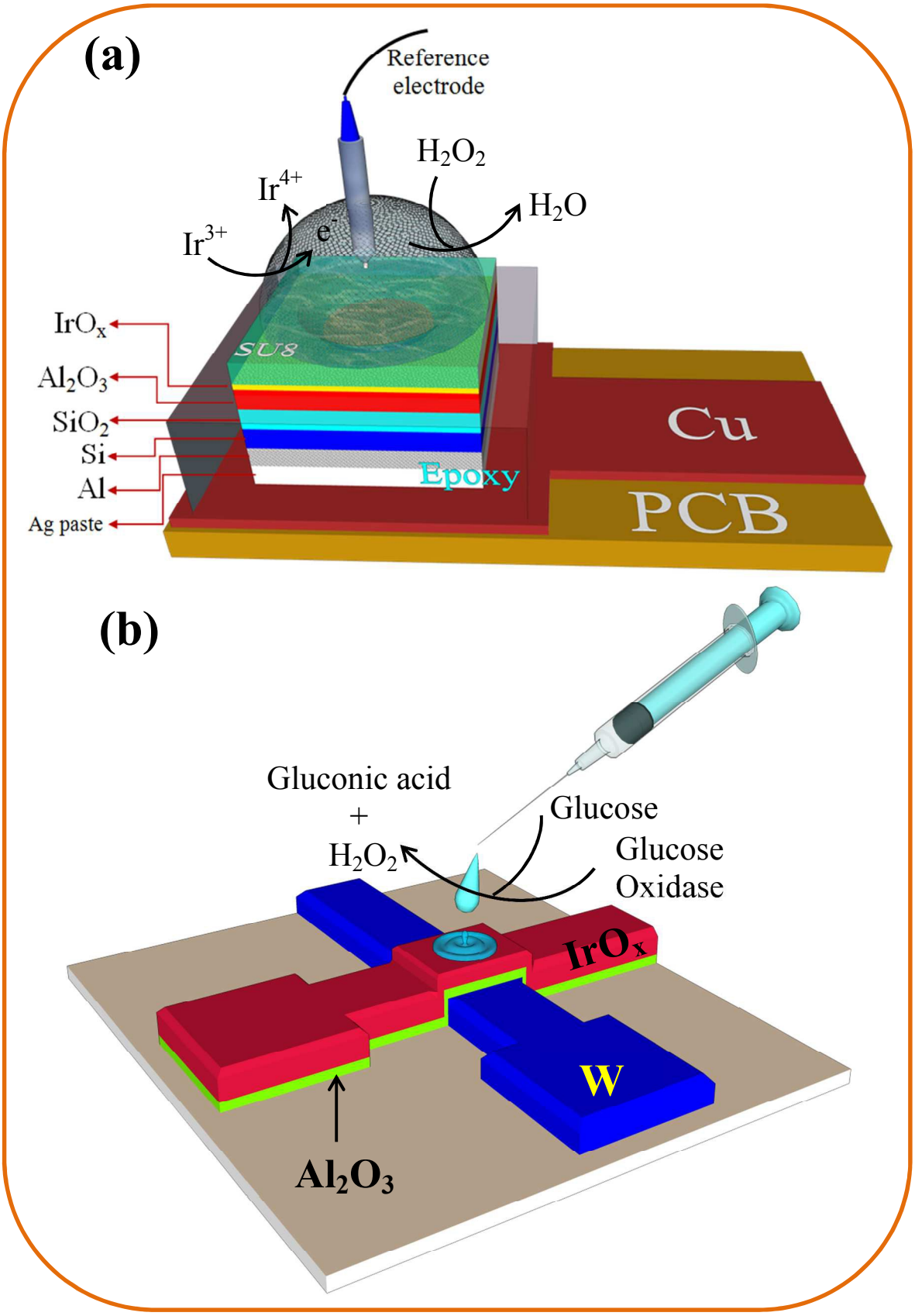


**Fig. 2. S. Chakrabarti et al., PCCP, July, 2017**

View Article Online
DOI: 10.1039/C7CP05089E



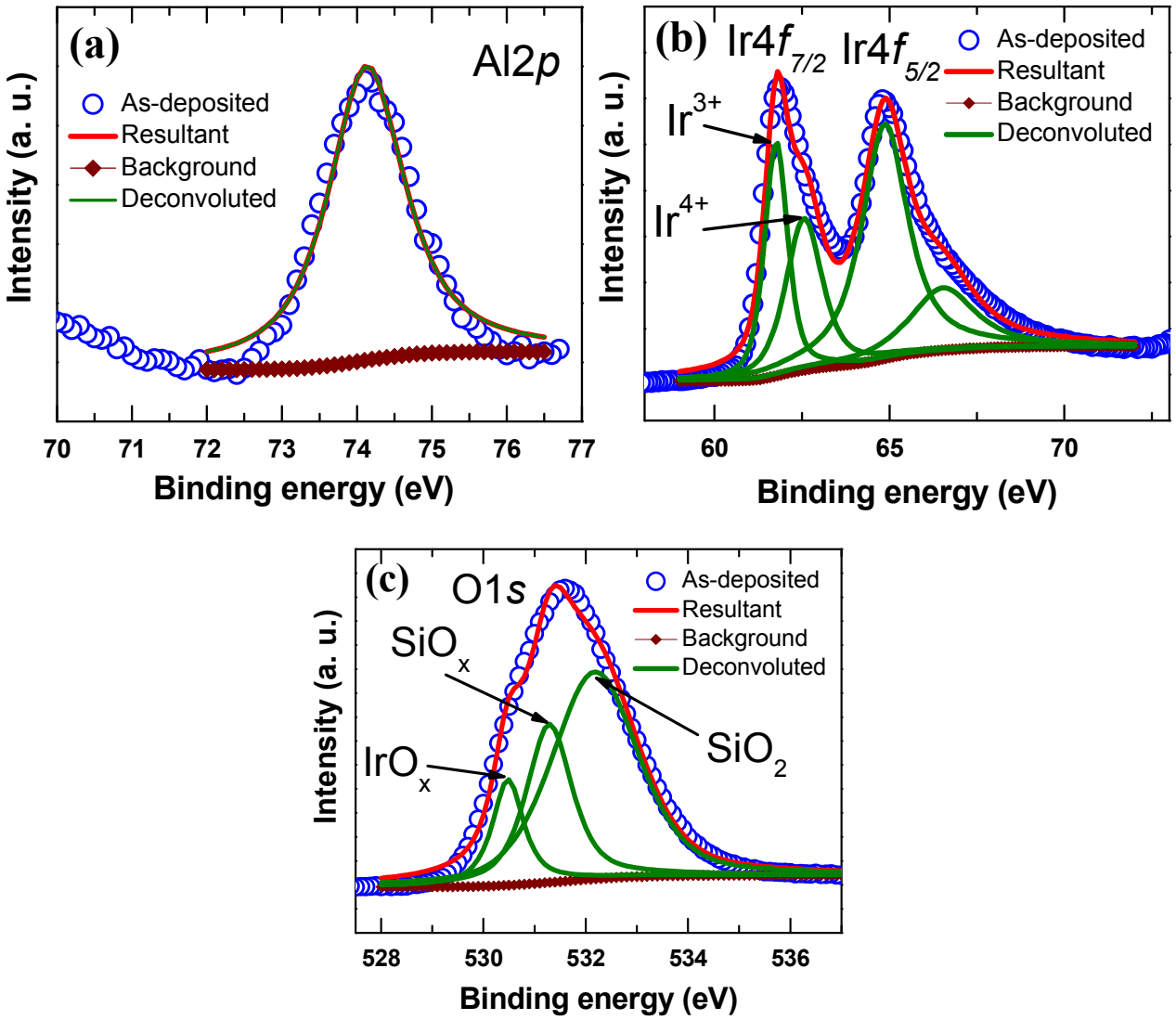


**Fig. 3. S. Chakrabarti et al., PCCP, July, 2017**

View Article Online
DOI: 10.1039/C7CP05089E



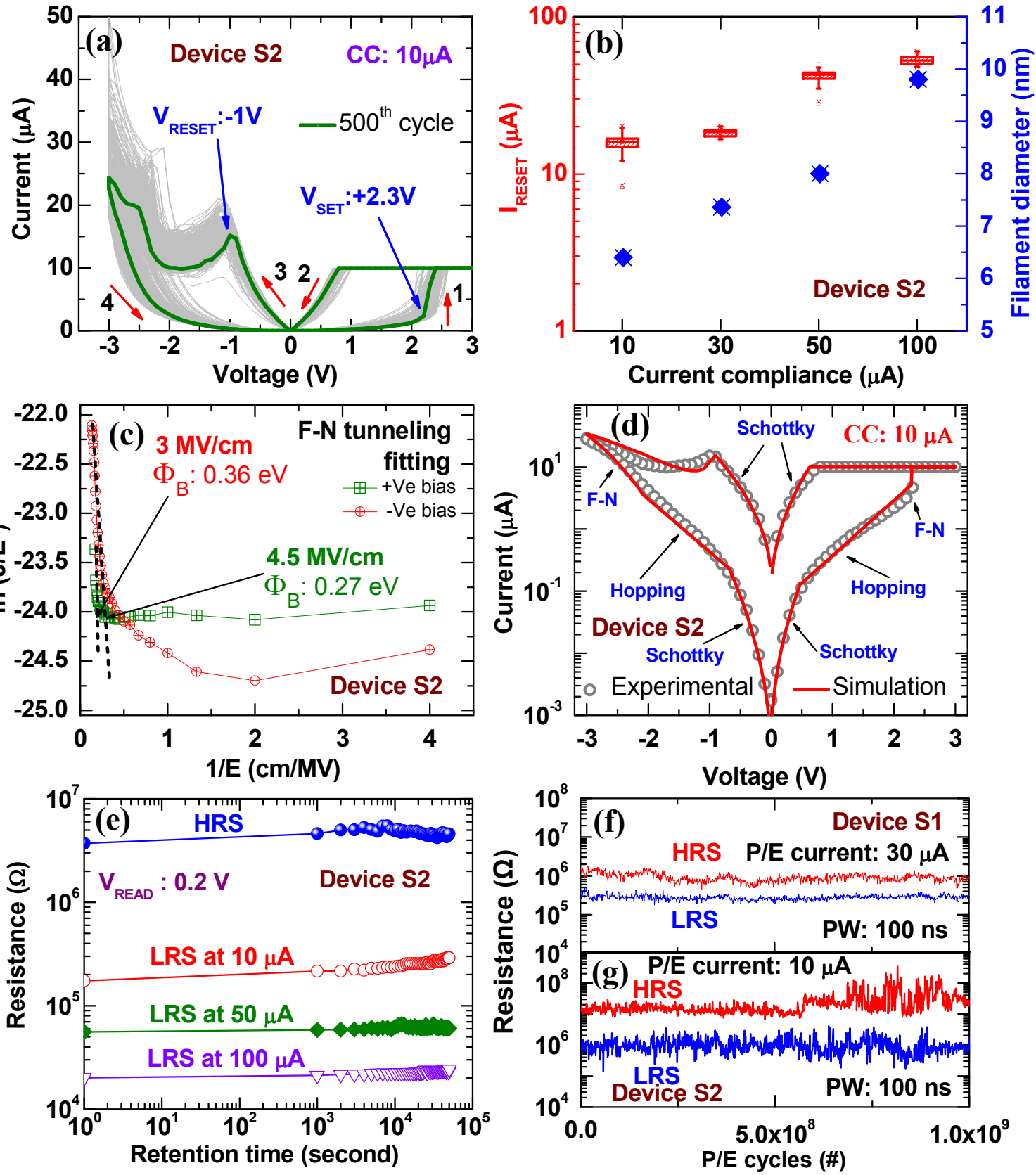


Fig. 4. S. Chakrabarti et al., PCCP, July, 2017

View Article Online
DOI: 10.1039/C7CP05089E



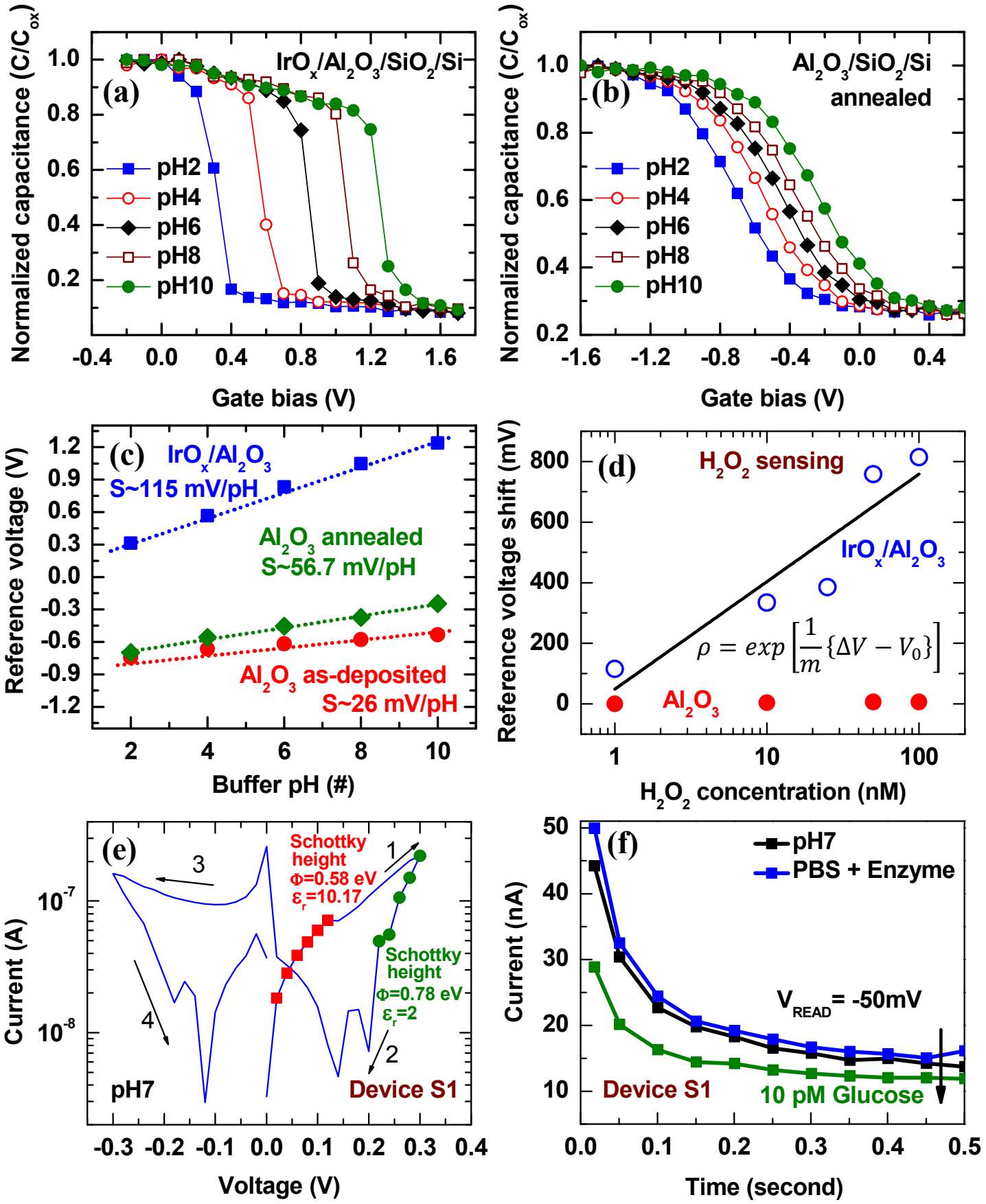


Fig. 5. S. Chakrabarti et al., PCCP, September, 2017